Nonlinear Photoelasticity to Explicate Acoustic Dephasing Dynamics

S. Lee,[1] H. Jeong,[1] H. Lee,[1] A. J. Minnich,[2] S.-R. Jeon,[3] T. H. Chung,[3] C. J. Stanton,[4] and Y. D. Jho[1, *]

[1]*School of Electrical Engineering and Computer Science,*
Gwangju Institute of Science and Technology, Gwangju 61005, Korea
[2]*Division of Engineering and Applied Science, California Institute of Technology, Pasadena, California 91125, United States*
[3]*LED Research and Business Division, Korea Photonics Technology Institute, Gwangju 61007, Korea*
[4]*Department of Physics, University of Florida, Gainesville, Florida 32611, United States*
(Dated: December 10, 2019)

Detection and controlling of acoustic (AC) phonon phase have been strenuous tasks although such capability is crucial for further manipulating thermal properties. Here, we present a versatile formalism for tracing AC nanowaves with arbitrary strain compositions by incorporating the nonlinear photoelasticity (PE) into ultrafast acoustics where broad AC spectrum encompassing thermally important THz frequency range should be collected far beyond Brillouin frequency. The initial AC phase upon displacive carrier generation could be inherently varied depending on the bipolar AC compositions by implementing externally biased piezoelectric diodes. The importance of adopting nonlinear PE is then manifested from the transient phase shift either abrupt at the point of diffuse surface scattering or gradual during phonon-phonon or phonon-electron scattering events based on which the ratio of nonlinear to linear PE coefficient is experimentally extracted as a function of the detection probe energy, reaching 0.98 slightly below the bandgap. As the probing energy is rather set away from the bandgap, AC phase is completely invariant with any scattering events, exhibiting the conventional trend at Brillouin frequency in linear regime. Under potent influence of nonlinear PE, the AC dephasing time during the propagation are quantified as a function of AC wavepacket size and further correlated with intrinsic and extrinsic AC scattering mechanisms in electron reservoir.

PACS numbers:

The emerging progress in precisely controllable thermal metamaterials requires the manipulations of wavy properties of phononic bands comprising thermal transport, particulary in a scale smaller than the phonon mean free path or phonon wavelengths [1], where the ability to measure and understand phase of phononic wavepackets could enable a wide range of applications [2]. The corresponding phase shift during the scattering events could be the key parameter influencing the thermal conductivity (κ) which varies in nanoscale [3], quality factors in optomechanical devices [4], cavity designs in phonon laser [5], and functionalities for phononic information processing [6]. In the context of thermal transport, acoustic (AC) phonon branches with frequency around a few THz decisively contribute to κ while the short lived optical phonons are less affecting in, e.g., bulk and thin films of Si [7]. The significance of identifying the AC phase in the thermally decisive spectral range has been, however, matched by its concomitant technical difficulties in clear contrast to sound manipulations [8]; the majority of device materials are yet to be investigated for correlating AC spectra with decay mechanisms and thermal transport even though the better heat dissipation are crucial for nanoscale devices [9].

From the detection viewpoint of ultrafast acoustics, the complex refractive index change $\Delta^\eta \tilde{n}$ under weak dynamic strain (η) determines differential reflectivity (transmission) spectra such that $\Delta R(t)/R$ ($\Delta T(t)/T$) $\propto F \cos(2\pi f_B t + \phi_0)\mathfrak{F}_\eta$ [10], where $f_B = 2nv_{AC}E_{probe}/hc$ with AC velocity v_{AC}, Plank constant h, probing laser energy E_{probe}, and c the speed of light. In this well-
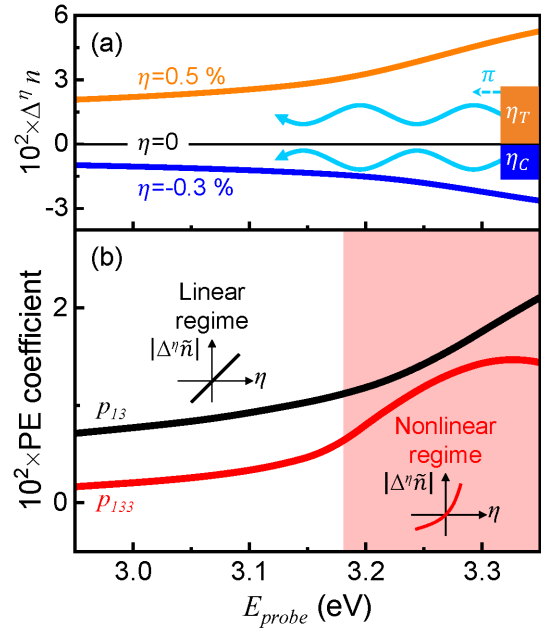

FIG. 1: (a) Strain-induced change in refractive index $\Delta^\eta n$ in bulk GaN as a function of E_{probe}. (b) Photoelastic coefficients of $\frac{\partial \epsilon}{\partial \eta}$ and $\frac{1}{2}\frac{\partial^2 \epsilon}{\partial \eta^2}$ as a function of E_{probe}.

established linear photoelasticity (PE) regime, the innate convolution between probe-beam interference patterns and $\Delta^\eta \tilde{n}$ restrict $\mathfrak{F}_\eta$, the Fourier component of $\Delta^\eta \tilde{n}$, at the Brillouin frequency of f_B, i.e., $\mathfrak{F}_\eta \sim \frac{1}{2\tilde{n}}\frac{\partial \epsilon}{\partial \eta}\mathfrak{F}(f_B)$

[10, 11], where ϵ is the dielectric constant of a crystal and $\mathfrak{F}$ denotes the Fourier transform of η. This linear criterion places a severe limitation on the range of f_B near 0.1 THz, unless otherwise incorporated with further specialized frameworks for zone-folded phonons [12] or AC echoes [13, 14]. Furthermore, the residual phase ϕ_0 is also fixed by the epicenter z_0 and the probe wavenumber whereas the sensitivity amplitude F was simplified by reflection (transmission) coefficient $R(T)$ at E_{probe} [11]. On the other hand, in the context of nonlinear phononics, $\Delta^\eta \tilde{n}$ is expanded with η into higher orders: $\Delta^\eta \tilde{n} \approx \frac{1}{2\tilde{n}}[\frac{\partial \epsilon}{\partial \eta}\eta + \frac{1}{2}\frac{\partial^2 \epsilon}{\partial \eta^2}\eta^2] + \bigcirc(\eta^3)$, where $\frac{\partial \epsilon}{\partial \eta}$ and $\frac{1}{2}\frac{\partial^2 \epsilon}{\partial \eta^2}$ are the linear and nonlinear PE coefficient, respectively. Then, $\mathfrak{F}_\eta$ is formulated to incorporate entire AC spectrum:

$$\mathfrak{F}_\eta \approx \frac{1}{2\tilde{n}}\frac{\partial \epsilon}{\partial \eta}\mathfrak{F}(f_B)[1 + \frac{1}{2}\frac{\partial^2 \epsilon}{\partial \eta^2}(\frac{\partial \epsilon}{\partial \eta})^{-1}\frac{\int_0^\infty df\mathfrak{F}(f)\mathfrak{F}(f_B - f)}{\mathfrak{F}(f_B)}] \quad (1)$$

in the nonlinear regime (See Supplementary Material for analytic expressions [15]). Please note that the nonlinear to linear ratio of PE coefficient $[\frac{1}{2}\frac{\partial^2 \epsilon}{\partial \eta^2}/\frac{\partial \epsilon}{\partial \eta}]$ is a weighting factor in the second term where the additional convolution incorporates the entire AC frequency (f) available for broad spectra. Thus, the nonlinear PE should infuse the previously restrained AC decay beyong f_B, as expected from the broad Fourier width ($\sim$4 THz) for coherent nanometric wavepacket with typical $v_{AC} \sim$8 nm/ps in crystals. Nonlinear phononics as formulated here are ambivalently applicable either to the anharmonicity with gigantic η such as supersonic speed change [16] and higher harmonic generations of phonons [17, 18] or to the nonlinear PE with reduced η.

In order to visualize the nonlinearity even in harmonic regime, we calculated the E_{probe}-dependent linear and nonlinear PE coefficients representatively in wurtzite GaN, by adapting the density functional theory (DFT) on optical properties [19] into nonlinear strain expansions. Figure 1(a) first examined the η-induced changes in n as a function of E_{probe} under the range of 0.5 % (-0.3 %) for the tensile (compressive) component η_T (η_C), locally generated from dynamic longitudinal AC (LA) wavepackets along the symmetric c axis. The sign of $\Delta^\eta n$ indicates that tensile-strain-induced probe reflections would have a phase shift by π upon reflection off AC wavefronts while no phase inversion in photon is expected by compressive strains [15], conveying the phase information of phonons into the light reflections. Thus, the optically detected AC phase can be manipulated by launching bipolar nanowaves with controllable strain compositions exemplarily in the piezoelectric diodes [20]. Figure 1(b) simulated E_{probe}-dependent the linear and nonlinear PE coefficients, extracted from $\Delta^\eta \tilde{n}$–η relation. As $\frac{1}{2}\frac{\partial^2 \epsilon}{\partial \eta^2}$ ($\equiv p_{133}$ in our symmetry) is approaching $\frac{\partial \epsilon}{\partial \eta}$ ($\equiv p_{13}$) up to $\sim$90 % at E_{probe} around 3.28 eV, the nonlinear PE regime is indeed experimentally accessible as denoted by the shaded E_{probe} range in clear contrast to linear PE
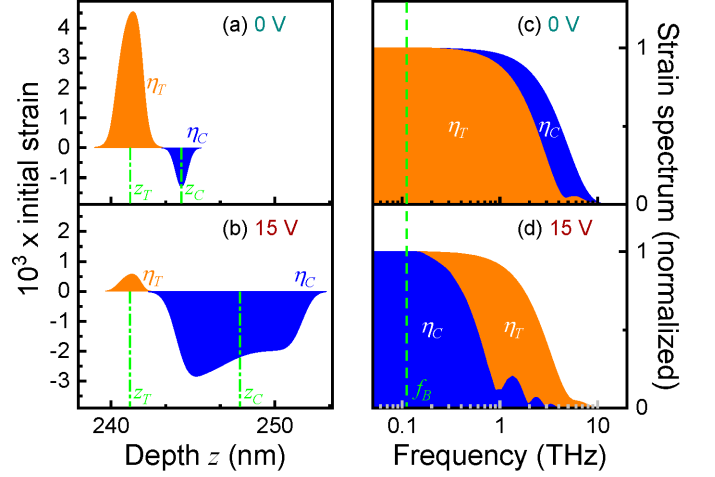

FIG. 2: Calculated strain profiles of η_T and η_C at (a) 0 V and (b) 15 V at the moment of generation (t=0 ps). Corresponding strain spectrum at (c) 0 V and (d) 15 V.

regime in lower energy sides ($<$3.2 eV).

In conjunction with spectrally broad nonlinear detection, when bipolar AC nanowaves with being launched from the epicenters z_T and z_C are measured by differential reflectivity spectra (DRS), η_T- and η_C-induced changes are superimposed incorporating their phase correlation: $\Delta R(t) = \Delta^{\eta_T} R(t) + \Delta^{\eta_C} R(t) \sim F A_{C/T} \cos(2\pi f_B t + \phi_0 + \phi_{C/T})$, where the bipolarity-induced amplitude modulation in DRS is

$$A_{C/T} \propto \mathfrak{F}_T([1 - (\mathfrak{F}_C/\mathfrak{F}_T)\cos(2nk(z_C - z_T))]^2$$
$$+ [(\mathfrak{F}_C/\mathfrak{F}_T)\sin(2nk(z_C - z_T))]^2)^{\frac{1}{2}} \quad (2)$$

and the corresponding additional phase shift in DRS is

$$\phi_{C/T} = \tan^{-1}[\frac{\sin(2nk(z_C - z_T))}{\cos(2nk(z_C - z_T)) - (\mathfrak{F}_C/\mathfrak{F}_T)^{-1}}]. \quad (3)$$

Here, $\eta_{T(C)}$-induced value of $\mathfrak{F}_\eta$ was obtained from Eq. (1) and symbolized as $\mathfrak{F}_{T(C)}$. Equation (2) and (3) generalize the phase and amplitude modulations of the DRS by three previously belittled parameters: (I) the strain compositions between tensile and compressive strains that adjusts $\mathfrak{F}_C/\mathfrak{F}_T$, (II) f-distributions of $\mathfrak{F}_T$ and $\mathfrak{F}_C$, and most importantly (III) the value of $\frac{1}{2}\frac{\partial^2 \epsilon}{\partial \eta^2}/\frac{\partial \epsilon}{\partial \eta}$ which links the THz spectral contribution to $\mathfrak{F}_\eta$ in Eq. (1).

In this letter, the bipolar strain compositions was continuously manipulated via a vertical electric field along c-axis upon femtosecond photo-carrier excitations in nanoscale InGaN/GaN piezoelectric diodes. The phase of AC nanowaves was transiently traced during AC reflections and propagation by measuring degenerate DRS at 293 K, representatively in the nonlinear regime of E_{probe} at 3.289 eV as compared to phase-invariant linear regime at 3.163 eV. The structures used in this work have the similar doping parameters with our previous works [20] to electrically manipulate the LA phonon mode under the
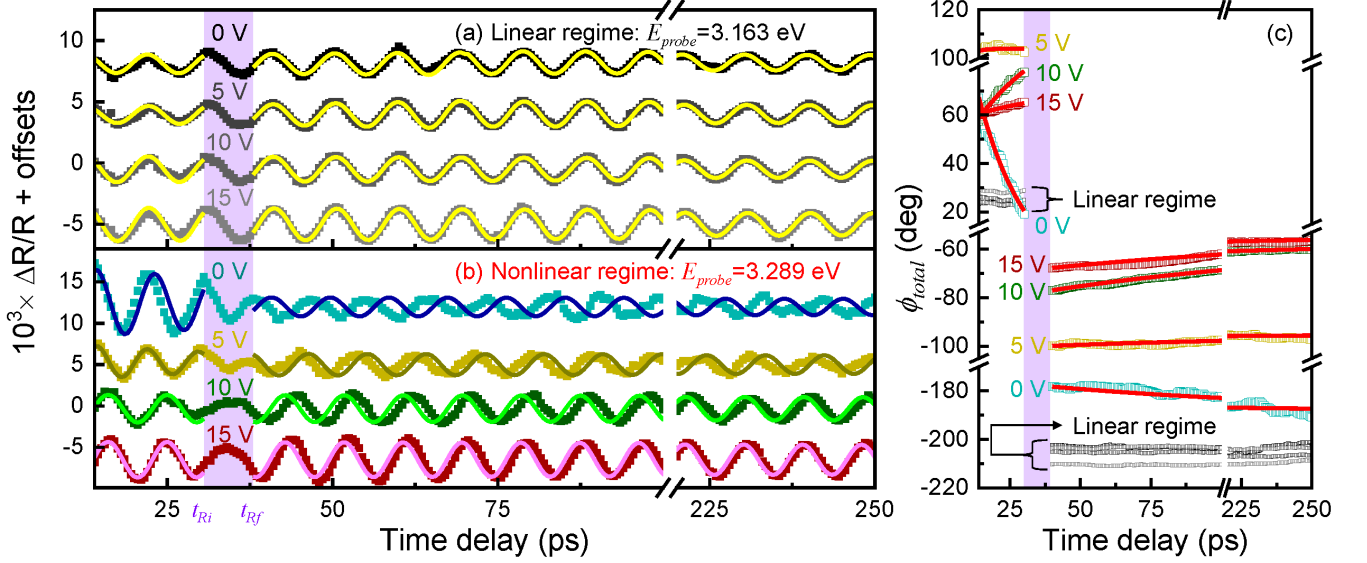
FIG. 3: The AC oscillations before ($t < t_{Ri}$) and after ($t > t_{Rf}$) the surface reflection (a) in the linear and (b) in the nonlinear PE regimes. The experimental data (scatters) were fitted with decaying cosine waves, where the frequency was fixed at the Brillouin scattering frequency f_B. (c) Extracted total phases ϕ_{total} of AC oscillations.

pumping fluence of ∼100 μJ/cm^2, but with higher piezo-electric fields (PEFs) in intrinsic region of 2.1 MV/cm in five 2.2 nm-thick In$_{0.15}$Ga$_{0.85}$N quantum wells (QWs) and of -1 MV/cm in four 10 nm-thick GaN barriers. The QWs were encased by p-GaN from the depth z=0 (air/p-GaN interface) to 200 nm, p-Al$_{0.1}$Ga$_{0.9}$N from z=200 to 230 nm, and n-GaN from z=281 nm to the sapphire substrate at z=4.281 μm, forming rectifying junction with the reverse voltage V_R below 22 V. The carrier concentrations of the main propagating medium of n-GaN was 3×10^{18} cm^{-3}. The inherent lattice-mismatch at QW-barrier interfaces caused the periodic normal strain variation with a wave vector of $2\pi/(L_w+L_b)$, launching not only the propagating LA wavepackets [21] but also zone-folded LA (ZFLA) phonons with a constant phase [15], where L_w and L_b are the QW and barrier widths, respectively.

To visualize V_R-dependent bipolar strain wavepackets, by considering photo-carrier distribution based on transition processes, calculated strain profiles of η_T (η_C) originated from QW (barrier) with the epicenter z_T (z_C) were plotted in figure 2(a) for 0 V and (b) for 15 V at the moment of generation (t=0 ps). In the linear regime, the pumping energy (E_{probe} in our degenerated scheme) was set to generate electron-hole pairs within QWs, consequently unipolar η_T was initially launched via spatially direct type I transitions [22]. On the other hand, when the excitation energy was in the nonlinear PE regime at 3.289 eV, the electrons could be excited also into the barriers within the exciton Bohr radius near interfaces through spatially indirect type II transitions, thus spatially narrow η_C also was launched in barriers side at 0 V with η_T. With increasing V_R, direct absorption within

the barriers became considerable via the enhanced Franz-Keldysh effect, as a result spatial width of η_C became broader keep up with the barrier width at 15 V (For more details, refer to transitions and concomitant transport processes for the photo-excited carriers [15]). In this regard, the spatial width and epicenter z_C of η_C were effectively varied with V_R compared to relatively unvarying η_T, and thus polarity of broad strain was converted from η_C to η_T with V_R. The spatial width of η_T (η_C) was estimated to be about 1.6 (0.8) nm at 0 V and 1.3 (7.4) nm at 15 V, respectively. By considering the propagation of AC nanowaves, corresponding spectral width of η_T (η_C) was estimated to be about 2.3 (4.1) THz at 0 V and 2.7 (0.6) THz at 15 V in figure 2(c,d), respectively. In this way, bipolar strain compositions were assigned by adjusting V_R, and consequently, not only $\mathfrak{F}_C/\mathfrak{F}_T$ values but also f-distributions of $\mathfrak{F}_\eta$ concomitantly were manipulated in nonlinear regime.

To confirm the aforementioned nonlinear detection under bipolar strains in DRS, the AC oscillations were extracted in figure 3 with differently colored scatters assigned to different V_R values in (a) linear and in (b) nonlinear regime. The initial time delay about 14 ps in Fig. 3 was chosen to exclude the earlier complicated phenomena such as the ZFLA phonons with constant phase estimated to be zero irrespective of different PE regimes or bipolar profiles and the carrier capturing dynamics with barrier-to-QW transports rather than ballistic transports, and consequently, to concentrate on the phase and amplitude with respect to propagating LA phonons hereafter (For more details, refer to phase analysis of ZFLA phonons and the correlation between capture dynamics and transient lineshapes in [15]). Fitting curves with convention-
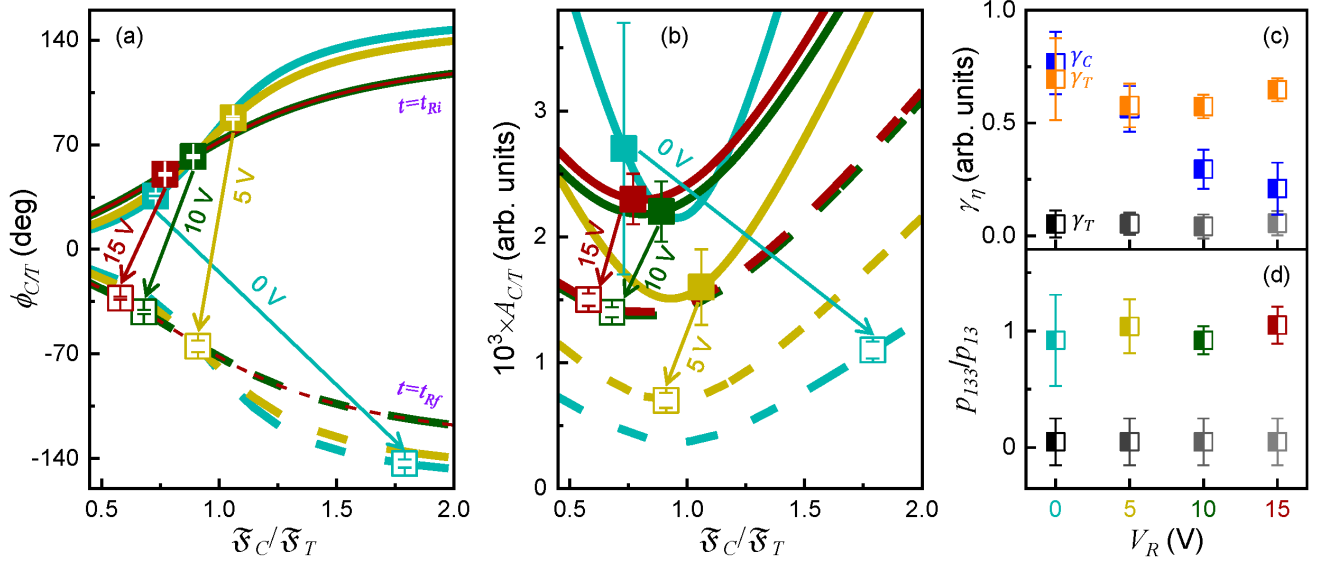
FIG. 4: Relation between $\mathfrak{F}_C/\mathfrak{F}_T$ and (a) $\phi_{C/T}$, (b) $A_{C/T}$ before ($t = t_{Ri}$) and after ($t = t_{Ri}$) the surface reflection in the linear and nonlinear regime based on z_C-z_T values (3.2, 4.0, 6.7 nm for 0, 5, 10~15 V). Estimated (c) decay rate γ_η and (d) $\frac{1}{2}\frac{\partial^2 \epsilon}{\partial \eta^2}/\frac{\partial \epsilon}{\partial \eta}$ (p_{133}/p_{13}) in the linear and nonlinear regime.

ally expected Brillouin frequency at f_B were guided with solid lines in linear regime with yellow lines and in nonlinear regime with V_R-dependent colors. In the fitting curves, the phases at t_{Rf} were set by deliberating on surface-reflection-induced phase shift from polarity inversion of strain and reversed propagation direction in conventional Brillouin oscillation with f_B=105.5 (112.0) GHz at E_{probe} of 3.163 (3.289) eV; during the reflection, the amount of phase jump was set to be 228° (242°) for linear (nonlinear) regime. By fixing the f_B extracted in early time delay before ($t < t_{Ri}$) and after ($t > t_{Rf}$) reflection, the total phases of AC oscillations were further extracted in figure 3(c). Then, the total phases were fitted based on exponentially-decaying $\phi_{C/T}$ assigned to red solid lines. Under unipolar strains the $\phi_{C/T}$ should be fixed either 0° for η_T or 180° for η_C in Eq. (3) regardless of PE regimes, and thus $\phi_{C/T}$ cannot be varied with V_R and time. As unipolar η_T was launched from QW without η_C at 3.163 eV, the total phases ϕ_{total} in linear regime of Fig. 3(a,c) were almost invariant with V_R and were well-matched with ϕ_0; in our structure, ϕ_0 was estimated to be about 22.7° for the unipolar η_T. Also, the fitting curves followed the experimental results over the entire temporal range, implying that f_B was time-invariant. On the contrary, in nonlinear regime of Fig. 3(b,c) under bipolar wavepackets, the drastic phase shift with V_R by ~48° at 14 ps was apparently ascribed to change in $\phi_{C/T}$: as bipolar strain compositions were manipulated by V_R, $\mathfrak{F}_C/\mathfrak{F}_T$ values were also varied with V_R in $\phi_{C/T}$ [Cf. Fig. 2(a,b)]. Notably, the experiments deviated from the fitting curves with time delay, indicating that $\phi_{C/T}$ also changed with time. The time-varying $\phi_{C/T}$ could be originated by changes of $\mathfrak{F}_C/\mathfrak{F}_T$ in Eq. (3)

through the different decay rates between $\mathfrak{F}_T$ and $\mathfrak{F}_C$. In other words, the time-dependent behaviors of $\phi_{C/T}$ cannot be explained without nonlinear PE in calculating $\mathfrak{F}_T$ and $\mathfrak{F}_C$ since AC decay rate at f_B (~0.1 THz) observable in linear regime is extremely small ($< 1/1.3$ ns) and is coincident for $\mathfrak{F}_T$ and $\mathfrak{F}_C$ to be seen during reflection [15, 25] and the propagation in the unbiased n-GaN [26]. Furthermore, time-dependent behaviors of $\phi_{C/T}$ that varied by V_R in nonlinear regime of Fig. 3(c), also cannot be explained without consideration for different AC decay rates between $\mathfrak{F}_T$ and $\mathfrak{F}_C$ in $\phi_{C/T}$ based on V_R-dependent f-distributions of bipolar strains [Cf. Fig. 2(c,d)].

By using phase shift and amplitude change during the surface reflection, the nonlinearity parameter $\frac{1}{2}\frac{\partial^2 \epsilon}{\partial \eta^2}/\frac{\partial \epsilon}{\partial \eta}$ was then quantified at 3.289 eV in figure 4. The V_R-dependent $\phi_{C/T}$ and $A_{C/T}$ values before (filled scatters) and after (empty scatters) the surface reflection were firstly plotted in Fig. 4(a,b) for the nonlinear regime. Considering the change of epicenter deviation between η_C and η_T (z_C-z_T values) with V_R in $\phi_{C/T}$ and $A_{C/T}$, calculation curves before (solid lines) and after (dashed lines) the surface reflection were also illustrated in Fig. 4(a,b). First of all, compared to invariant phase with V_R in linear regime, in nonlinear regime $\phi_{C/T}$ at t_{Ri} manifested actively manipulated strain compositions with V_R. Then, the phase jumps t_{Rf} closely related to AC dynamic during the surface reflection, where the AC wavepackets underwent polarity inversion and the diffuse-scattering. As the strain polarity was reversed during the reflection, the sign of $\phi_{C/T}$ should be varied in Eq. (3) with corresponding inversion of $\mathfrak{F}_C/\mathfrak{F}_T$ value. In addition, since the Kapitza specular
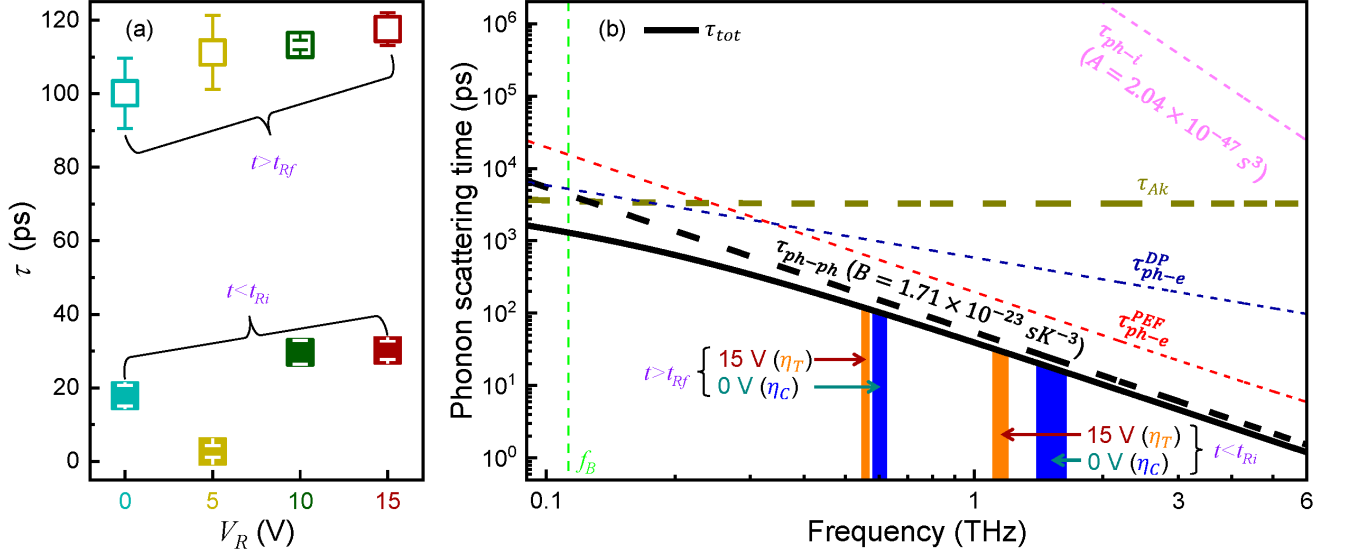
FIG. 5: (a) Extracted dephasing time τ before reflection (filled square) and after reflection (empty square) with V_R. (b) Estimated phonon scattering time τ_{phonon}.

scattering was discussed in f-dependent attenuation of the specularity parameter $p=e^{-16\pi^2\delta^2 v_{AC}^{-2}f^2}$ [13, 25], η_T and η_C were significantly decayed during the surface reflection; considering surface roughness δ (0.7 nm), diffuse-scattering rate was 50 % at around 0.75 THz. As AC detection range was limited at f_B ($\sim$0.1 THz) in linear regime diffuse-scattering rates between η_T and η_C were identical in spite of significant decay and different f-distribution of η_T and η_C, and thus, $\mathfrak{F}_C/\mathfrak{F}_T$ in $\phi_{C/T}$ cannot be varied except for inversion of $\mathfrak{F}_C/\mathfrak{F}_T$. On the contrary, with spectrally broad AC detection, the f-dependent diffuse-scattering rate caused an additional change in $\mathfrak{F}_C/\mathfrak{F}_T$ value based on the f-distribution of strain. At t_{Rf}, the phase jumps deviated from the polarity inversion-induced $\phi_{C/T}$ with increased (decreased) $\mathfrak{F}_C/\mathfrak{F}_T$ for 0 V (others) as denoted by the right-pointing arrow (left-pointing arrow) in Fig. 4(a), because of the different diffuse-scattering rate between η_T and η_C. Interestingly, increasing $\mathfrak{F}_C/\mathfrak{F}_T$ at 0 V was originated by the larger diffuse-scattering rate of η_C induced serious decrement in η_C because its spatial width (0.8 nm) was rather comparable to the δ, and also confirmed in significant decay of $A_{C/T}$. On the contrary, as the polarity of spectrally broad strain was varied from η_C to η_T with V_R, $\mathfrak{F}_C/\mathfrak{F}_T$ was decreased at other bias due to the relatively narrow spatial width of η_T. By comparing both the $\phi_{C/T}$ and $A_{C/T}$ values at t_{Ri} with those at t_{Rf} based on the Eqs (2) and (3), the $\mathfrak{F}_\eta$ values were extracted in nonlinear regime. Based on that, the decay rate of η_T (η_C) generated from QW (barrier) in nonlinear regime was introduced as $\gamma_T=(\mathfrak{F}_T(t_{Ri})-\mathfrak{F}_C(t_{Rf}))/\mathfrak{F}_T(t_{Ri})$ ($\gamma_C=(\mathfrak{F}_C(t_{Ri})-\mathfrak{F}_T(t_{Rf}))/\mathfrak{F}_C(t_{Ri})$) in Fig. 4(c). First of all, compared to γ_T (black scatters) values corresponding

diffuse-scattering rate in linear regime, extremely large γ_T (blue scatters) and γ_C (orange scatters) values were contributed by nonlinear PE coefficient; considering δ, diffuse-scattering rate was 1.6 % at f_B. In addition, gradually decreasing behavior of γ_C with V_R in nonlinear regime implies that spectral width of η_C also decreased, which well matches with spatially broadened η_C with V_R at 3.289 eV. On the other hand, with V_R, relatively stationary γ_T values originated from maintaining the spatial width of η_T within QW width. The extracted decay rate, in this way, could be compared with the modified high-f contribution in Eq. (1), by setting $\frac{1}{2}\frac{\partial^2\epsilon}{\partial\eta^2}/\frac{\partial\epsilon}{\partial\eta}$ as a variable, allowing averaged value of 0.98$\pm$0.23 as illustrated in Fig. 4(d). Please note the quantitative agreement of nonlinear PE coefficient with DFT-mediated results in Fig. 1(b) in spite of concomitantly large error due to tracing the variation of the broad spectral width of η_C in the 0 V case. In the linear regime, as implied from persistent ϕ_0 regardless of reflection, γ_T was $\sim$0.05% throughout bias range and the corresponding $\frac{1}{2}\frac{\partial^2\epsilon}{\partial\eta^2}/\frac{\partial\epsilon}{\partial\eta}$ $\sim$0.06 was ignorably small within the error range [15].

Aforementioned time-varying AC phase as measured in Fig. 3(b,c) can be further correlated with the f-dependent scattering mechanisms. During the propagation of AC nanometric waves firstly toward the surface then toward the electron reservoir, the intrinsic and extrinsic scattering processes should modify $\phi_{C/T}$ in Eq. (3) via the nonlinear PE whose values are extracted as $\phi_{C/T}(t)=\phi_{C/T}(t_0)+\phi_s[1-e^{-(t-t_0)/\tau}]$ (as guided by red solid lines in Fig. 3(c)), where t_0 indicates the initial time-delay of the phase detection ($\sim$14 ps before reflection; $\sim$38 ps after reflection). Then, the fitting parameters τ (ϕ_s) represents the duration (amount) of the phase

changes and τ were summarized in Fig. 5(a) (For more details, refer to Sec. VIII in [15]). Interestingly, in linear PE regime, ϕ_0 was contrasted to be invariant without sensing the high f-component. Also, since transient $\phi_{C/T}$ originates from the scattering-induced modification in $\mathfrak{F}_C/\mathfrak{F}_T$ accessible via nonlinear PE, the τ corresponds to the dephasing time of AC wavepackets. With substantial $\frac{1}{2}\frac{\partial^2\epsilon}{\partial\eta^2}/\frac{\partial\epsilon}{\partial\eta}$, $\mathfrak{F}_C$ is expected to decay faster than $\mathfrak{F}_T$ through f-dependent scattering processes due to ~ 2 times wider spectral width of η_C than that of η_T at 0 V [Cf. Fig. 2(a,c)], and thus the largest decrement of $\phi_{C/T}$ in Fig. 3(c) originated by rapid decay of $\mathfrak{F}_C$ with relatively short τ in Fig. 5(a) before the surface reflection. On the other hand, since η_T became narrow than η_C due to the spatially broadened η_C with V_R, $\phi_{C/T}$ increased with relatively small amounts except for 0 V in Fig. 3(c). From that point of view, the minute increase of $\phi_{C/T}$ at 5 V in Fig. 3(c) could be ascribed to the point at which the spatial width of η_C similar to that of η_T as η_C was widening. Accordingly, as the spectral width of widest $\mathfrak{F}_\eta$ decreased with V_R, corresponding τ increased due to f-dependent scattering processes. After the surface reflection, under the potent influence of diffuse scattering the bandwidth of $\mathfrak{F}_C$ and $\mathfrak{F}_T$ became similar and reduced at around 660 GHz regardless of spectral width at the moment of generation [15]. In accordance with similar bandwidth, the scattering-induced change in widest $\mathfrak{F}_\eta$ also became similar at all V_R, thus stationary τ values were estimated te be ~ 110 ps in Fig. 5(a). The dephasing time of spectrally broad packets could be used for mapping f-specific scattering times in the nonlinear PE formalism based on Eq. (1) and Eq. (3) as summarized in Fig. 5(b) (For mathematical details, refer to Sec. VIII [15]). The intrinsic and extrinsic scattering times decreases with f but in different ways as theoretically investigated; the intrinsic anharmonic scattering rate is $\tau_{ph-ph}^{-1}=BT^3\omega^2$ [26], where B is the three phonon scattering coefficient, T is the temperature, and ω corresponding to $2\pi f$; the other processes such as Akhiezer relaxation [27], impurity-phonon scattering [26], electron-phonon scattering via deformation potential coupling [28] and via piezoelectric coupling [29] are also differently f-dependent as summarized in [15]. For simplicity's sake, scattering times for the Akhiezer model, impurity-phonon scattering, and electron-phonon scattering were calculated based on doping density, mass difference to estimate the upper limit for the intrinsic anharmonic scattering rate; in this way, B was $<1.71\times10^{-23}$ sK^{-3} in our nonlinear regime with p_{133}/p_{13} of 0.98. Whereas, recently reported upper limit on B is still variant from 6×10^{-23} sK^{-3}[30] to 0.75×10^{-23} sK^{-1}[31] or 0.103×10^{-23} sK^{-1}[32], measured from transient amplitude lineshape in selected f-component in linear PE scheme. The upper limit of B should be larger than realistic B values of solids since the various extrinsic processes should be simultaneously influential. By applying

the estimated B value into scattering time calculation, τ values at 0 V (17.8 ± 2.8 ps) and 15 V (30.2 ± 2.4 ps) were dominated by the scattering at ~ 1.51 THz (blue shades) and ~ 1.15 THz (orange shades), respectively. However, the narrowed AC spectral shape after diffusive surface scattering (Cf. the abrupt $\phi_{C/T}$ jump in Fig. 4 during reflection) reveals the longer τ values at 0 V (100.1 ± 9.6 ps) and 15 V (117.6 ± 4.4 ps) which matched with ~ 610 GHz (blue shades) and ~ 560 GHz (orange shades), respectively. Please note this estimation of main f-component in dephasing process is associated with the pivotal role of scattering-dependent spectral profiles in setting $\mathfrak{F}_\eta$ (See [15] for more details, calculated by simultaneously applying f-dependent scattering and concomitant variation in $\mathfrak{F}_C/\mathfrak{F}_T$).

In conclusion, we demonstrated that the optically detected phase of AC nanowaves are sensitive to nonlinear PE depending on probe energies and can be actively manipulated by strain compositions. When phonons were probed in the linear regime, no phase shift with reflection or time delay was observed in AC oscillations. On the contrary, in the nonlinear regime the dephasing was identified and correlated with the scattering at the surface. The direct and transient measurement of AC dephasing processes, if combined with the emergent design and fabrication capability for THz phonon branches, could be utilized as an important linkage between thermal engineering and ultrafast phononic detection schemes.

---

* Electronic address: jho@gist.ac.kr
[1] See, e.g., A. Minnich et al., Phys. Rev. Lett. **107**, 095901 (2011).
[2] See, e.g., M. Maldovan, Nat. Mater. **14**, 667 (2015).
[3] M. N. Luckyanova et al., Science **338**, 936 (2012).
[4] Q. P. Unterreithmeier et al., Phys. Rev. Lett. **105**, 027205 (2010).
[5] See, e.g., A. Fainstein et al., Phys. Rev. Lett. **110**, 037403 (2013).
[6] F. Li et al., Nat. Commun. **5**, 5311 (2014).
[7] X. Wang and B. Huang, Sci. Rep. **4**, 6399 (2014).
[8] See, e.g., R. Martinez-Sala, J. Sancho, J. V. Sanchez, V. Gomez, J. Llinares, Nature 378, 241 (1995).
[9] See, e.g., Z. Yan et al., Nat. Commun. **3**, 827 (2012).
[10] C. Thomsen et al., Phys. Rev. B **34**, 4129 (1986).
[11] R. Liu et al., Phys. Rev. B **72**, 195335 (2005).
[12] C.-K. Sun et al., Phys. Rev. Lett. **84**, 179 (2000).
[13] Y.-C. Wen et al., Phys. Rev. Lett. **103**, 264301 (2009).
[14] B. Liao et al., Nat. Commun. **7**, 13174 (2016).
[15] See Supplemental Material for the detailed mathematical formalisms based on which the experimental results

in differently strained samples were further elucidated for confirming the consistency of nonlinear PE. Additionally, the bias-dependent photocarrier capture dynamics under the different absorption types in quantum wells, the probe-energy-dependent quantification of nonlinear PE cofficient, and bias-dependence of transient zone-folded phonons are detailed in conjunction with the dynamic strain profiles from displacive carrier generation under the Franz-Keldysh effect.

[16] C. Klieber *et al.*, Phys. Rev. Lett. **114**, 065701 (2015).
[17] A. Bojahr *et al.*, Phys. Rev. Lett. **115**, 195502 (2015).
[18] A. Hoegen *et al.*, Nature **555**, 79 (2018).
[19] D. Cai *et al.*, J. Phys. D Appl. Phys. **42**, 185107 (2009).
[20] H. Jeong *et al.*, Phys. Rev. Lett. **114**, 043603 (2015); H. Jeong *et al.*, Phys. Rev. B **94**, 024307 (2016).
[21] J. S. Yahng *et al.*, Appl. Phys. Lett. **80**, 4723 (2002).
[22] Y. D. Jho *et al.*, Phys. Rev. B **66**, 035334 (2002).
[23] P. W. M. Blom *et al.*, Phys. Rev. B **47**, 2072 (1993).
[24] G. Vaudel *et al.*, Phys. Rev. B **90**, 014302 (2014).
[25] J. M. Ziman, Electrons and Phonons: The Theory of Transport Phenomena in Solids, Oxford University Press, Oxford, UK, 1960.
[26] C. Herring, Phys. Rev. **95**, 954 (1954).
[27] A. A. Maznev *et al.*, Appl. Phys. Lett. **102**, 041901 (2013).
[28] A. AlShaikhi *et al.*, Phys. Rev. B **81**, 195320 (2010).
[29] A. R. Hutson *et al.*, J. Appl. Phys. **33**, 40 (1962).
[30] T.-M. Liu *et al.*, Appl. Phys. Lett. **90**, 041902 (2007).
[31] F. J. Wei *et al.*, Sci. Rep. **6**, 28577 (2016).
[32] P.-A. Mante *et al.*, Ultrasonics **56**, 52 (2015).
[33] K. H. Lin, C. M. Lai, C. C. Pan, J. I. Chyi, J. W. Shi, S. Z. Sun, C. F. Chang, and C. K. Sun, Nat. Nanotech. 2, 704 (2007).